Multi-component ionic diffusion and proton adsorption in charged γ-alumina structures: Dynamic modeling and experimental study

Rita Fayad[1] · Yu-Yen Ting[2] · Françoise Couenne[1] · Christian Jallut[1] · Aurelie Galfré[1] · Elsa Jolimaitre[3] · Loïc Sorbier[4] · Charles-Philippe Lienemann[4] · Mélaz Tayakout-Fayolle[1]

Abstract

γ-alumina is highly employed as support for hydrotreatment catalysts prepared by impregnation and as adsorbent in water treatment. These applications consist of contacting γ-alumina with aqueous solutions, leading to the transport of ions inside the alumina pores and their adsorption on the pore surface. These physicochemical phenomena are governed by the γ-alumina pore surface and the solution characteristics. Predicting the physicochemical phenomena at the liquid/solid interface is crucial to optimize the design of catalysts and of water treatment adsorption processes. However, this is very challenging using conventional analytical techniques. In this work, the diffusion of protons and their counter-ions inside γ-alumina pores and the adsorption of protons on the pore surface are modeled at unsteady state during contact with acid solutions at different initial pH levels. Diffusion inside pores is represented using a combination of the zero current method and the Poisson-Boltzmann equation, while the proton adsorption is described by the Langmuir adsorption isotherm. Simulations agree well with the results of proton adsorption experiments in a batch system. The model accurately predicts the distribution of species inside the electrostatic double layer at the liquid/solid interface. It also computes the surface charge and the maximal adsorption capacities of different types of hydroxyl sites present on the alumina pore surface; both are very difficult to determine experimentally. This model can serve as a guide for the comprehension of the liquid/solid interface inside γ-alumina structures and their interaction with aqueous solutions during the initial stages of impregnation.
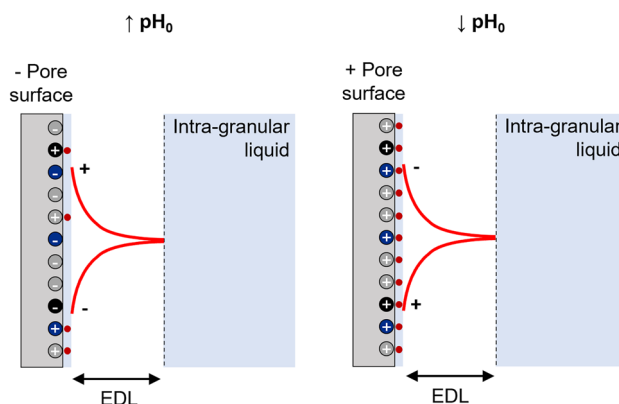
Keywords Adsorption · Alumina · Diffusion · Liquid/solid interface · pH · Surface charge

Abbreviations

DFT	Density functional theory
EDL	Electrostatic double layer
H^+	Protons
HNO_3	Nitric acid
MUSIC	Multisite complexation model
NO_3^-	Nitrate ions
OH	Hydroxyl groups
OH^-	Hydroxide ions
PZC	Point of zero charge

List of symbols

A	Debye-Hückel constant, $0.5085 M^{-1/2}$
a_p	Pore surface area per unit of pore volume or interfacial pore area, $m^2 m^{-3}$
$b_{i,j}$	Langmuir constant or the equilibrium adsorption constant of i on site j for H^+, $m^3 mol^{-1}$
C_i^{EDL}	Concentration of i inside the electrostatic double layer, $mol\ m^{-3}$
$\overline{C}_i^{EDL}$	Mean value of C_i^{EDL} with respect to the z direction, $mol\ m^{-3}$
C_i^f	Concentration of i in the extra-granular liquid phase, $mol\ m^{-3}$
C_i^{film}	Concentration of i at the interface between the intra-granular liquid phase and the pore surface, $mol\ m^{-3}$
C_i^p	Concentration of i in the intra-granular liquid phase, $mol\ m^{-3}$
$D_{eff,i}^p$	Effective diffusion coefficient of i, $m^2 s^{-1}$
$D_{m,i}^p$	Molecular diffusion coefficient of i in water, $m^2 s^{-1}$
EC	Electrical conductivity in the extra-granular liquid phase, $\mu S\ cm^{-1}$
F	Faraday's constant, $96{,}500\ C\ mol^{-1}$
I^j	Ionic strength in phase j, $mol\ L^{-1}$
K^{EDL}	Mass transfer coefficient in the intra-granular liquid phase or internal mass transfer coefficient, $m\ s^{-1}$
K^f	Mass transfer coefficient in the extra-granular liquid phase or external mass transfer coefficient, $m\ s^{-1}$
K_w	Water dissociation constant at 25°C, $10^{-8} mol^2 m^{-6}$
L	Average length of alumina extrudates, m
n	Total number of ionic species in solution
N	Number of types of active hydroxyl sites
N_i^{EDL}	Mass transfer flux of i from the intra-granular liquid phase to the pore surface or internal mass transfer flux, $mol\ m^{-2} s^{-1}$
N_i^f	Mass transfer flux of i from the extra-granular liquid phase to the intra-granular liquid phase or external mass transfer flux, $mol\ m^{-2} s^{-1}$
N_i^p	Molecular diffusion flux of i in the liquid intra-granular phase, $mol\ m^{-2} s^{-1}$
pK_a	Protonation constant
q_i	Total concentration of i adsorbed on all the adsorption sites, $mol\ m^{-2}$
$q_{i,j}$	Concentration of i adsorbed on the site j or the concentration of occupied hydroxyl sites of the type j on the alumina surface, $mol\ m^{-2}$
$q_{max,j}$	Maximal adsorption capacity of the site j or the maximal number of vacant adsorption sites of type j per unit of surface area, $mol\ m^{-2}$

r	Radial position inside extrudate or space direction parallel to the pore surface, m
R	Ideal gas constant, $8.314\ J\ mol^{-1} K^{-1}$
R_e	Radius of alumina extrudates, m
R_p	Pore radius of alumina extrudates, m
S_{BET}	Specific surface area of alumina extrudates, $m^2 g^{-1}$
t	Time, s
T	Temperature of the solution, K
$U^\parallel$	Electrostatic potential in the liquid intra-granular phase defined in the direction r parallel to the pore surface, V
$U^\perp$	Electrostatic potential in the electrostatic double layer defined in the direction z perpendicular to the pore surface, V
V_{BJH}	Pore volume of alumina extrudates, $m^3 g^{-1}$
V_f	Liquid volume, m^3
V_s	Volume of cylindrical alumina extrudates, m^3
z	Space direction perpendicular to the pore surface, m
z_j	Charge of the occupied adsorption site j
z_{sj}	Charge of the vacant adsorption site j

Greek letters

α	Intermediate variable in the expression of $U^\perp$, m^{-1}
γ_i^j	Activity coefficient of i in the phase j
$\Lambda_{m,i}$	Molar conductivity of i, $m^2\ S\ mol^{-1}$
ε	Dielectric constant or permittivity of the water solvent at 25°C and 1 atm, $6.94 \times 10^{-10}\ C\ V^{-1} m^{-1}$
ε_f	Fraction of the intra-granular liquid phase volume dedicated to the electrostatic double layer
ε_p	Porosity of alumina extrudates
λ	Thickness of the electrostatic double layer, m
μ_1	Singly coordinated or terminal OH sites or $\mu_1 - OH^{-0.5}$
μ_2	Doubly coordinated or bridged OH sites or $\mu_2 - O^{-0.75}$
μ_3	Triply coordinated or tri-bridged OH sites or $\mu_3 - O^{-0.5}$
ν_i	Valence of species i
ρ	Charge density of the liquid part of the electrostatic double layer, $C\ m^{-3}$
$\rho_{alumina}$	Apparent density of alumina extrudates, $g\ m^{-3}$
σ	Charge on the alumina pore surface, $C\ m^{-2}$

Superscripts

EDL	Electrostatic liquid double layer in contact with the pore surface
f	Extra-granular liquid
p	Intra-granular liquid

1 Introduction

γ-Alumina solids are highly used in industry as supports for hydrotreatment catalysts and as adsorbents in water treatment applications, due to their low cost, high specific surface area, and porous structure [8, 31]. Hydrotreatment catalysts are commonly prepared using the impregnation technique [30]. Both the impregnation of alumina solids with active species and their use as adsorbents in water treatment consist of contacting γ−alumina structures with aqueous solutions containing metallic ions. During this contact, the mass transfer of the ionic species in solution and their adsorption on the alumina pore surface occur. The interactions of the γ-alumina surface with aqueous solutions depend on the properties of: (i) the alumina pore surface (i.e., the charge and initial state) and (ii) the solution (i.e., the pH and metal concentration) [12, 29]. These interactions greatly influence the physicochemical phenomena at the liquid/solid interface. Understanding these phenomena and predicting the retention of species at the interface is paramount to improve the design of hydrotreatment catalysts via the impregnation technique and the efficiency of adsorption processes used in water treatment [10, 30].

Many researchers attempted the physical characterization of the alumina surface and the water/solid interface using spectroscopic techniques [13, 14]. Years of research showed that the γ-alumina surface consists of several types of hydroxyl (or OH) sites due to imperfections in the crystal structure [15, 29]. At least three groups of OH sites with different adsorption properties have been identified: (1) singly coordinated or terminal OH sites referred to as μ_1 (where the oxygen atom is bound to one aluminum atom), (2) doubly coordinated or bridged OH sites referred to as μ_2 (where the oxygen atom is bound to two aluminum atoms), and (3) triply coordinated or tri-bridged OH sites referred to as μ_3 (where the oxygen atom is bound to three aluminum atoms) [6, 13, 14]. When γ-alumina structures are contacted with water, the surface OH sites can act as Brønsted acids or bases [12] or as Lewis acids [19] and undergo transfer reactions with the protons in solution [6, 15, 29]. At low (high) pH, the OH sites are protonated (deprotonated) and become positively (negatively) charged [29]. The charging behavior of OH sites is highly dependent on the pH and ionic strength of the solution [38]. However, γ-alumina is a poorly crystalline and metastable oxide rendering the speciation of its surface rather challenging using conventional techniques [10]. As a result, there is still a lack of atomic scale understanding of the liquid/solid interface inside the γ-alumina pores during interactions with aqueous solutions [30] (e.g., impregnation with metallic salts or adsorption in water treatment).

Atomistic models at the liquid/solid interface could allow for a better comprehension of the γ-alumina pore surface. [33, 42, 43] introduced the classical one site—two pK and one site—one pK site binding models to describe the charging behavior of OH groups on the surface of amorphous and poorly crystalline mineral oxides at equilibrium. Yet, these models do not offer a detailed description of the phenomena at the solid surface since they do not differentiate between the surface sites [10].

Later on, [15] developed the MUltiSIte Complexation (or MUSIC) model to account for the heterogeneity of the surface OH sites. It allows for a prediction of the protonation constants (or pK_a) of surface OH sites on mineral oxides based on their effective charges and using the Poisson-Boltzmann equation. The latter has been used in literature to predict the surface charges of complex oxides in water, as has been done by [1, 29, 32, 38, 40, 44]. The Poisson-Boltzmann equation describes the electrostatic interactions between charged species in a solution and a charged surface and predicts the equilibrium distribution of ionic species inside electrostatic double layers (or EDL) formed at the liquid/solid interface to neutralize the surface charges (inside which all the species are assumed to adsorb in one plane) [16, 18]. It is based on the combination of Gauss' law and the Boltzmann distribution of ions at equilibrium with respect to the electrical potential obtained by assuming the chemical potentials of ions within the double layer to be equal to those outside of the EDL. Even though solving this equation might be complex, it can delineate the distribution of species near the charged surface [18].

More recently, complex density functional theory (or DFT) calculations have been successfully performed to obtain a detailed atomic description of the structure of the γ-alumina surface and the liquid/solid interface using thermodynamics [10, 13, 14, 30, 36, 37]. Reference [14] proposed a model for the monolayer chemisorption of water molecules in the vapor phase on well-identified OH sites located on the three most relevant plane orientations of the γ-alumina surface, as a function of temperature and pressure. They were able to determine the nature of the surface OH sites in the (100) and (110) planes and quantify them. Reference [30] analyzed the interaction of OH sites on the predominantly exposed (100) and (110) planes of the γ-alumina surface with liquid water molecules at 300 K. They found that the nature of any OH site and its network of hydrogen bonds to be the key factors governing the interactions with water. [10] combined DFT calculations with the basic Stern model to compute the surface charges of different OH sites at the liquid/solid interface as a function of the solution pH. However, DFT calculations could only provide theoretical insights about the properties of the γ-alumina surface in contact with water at short time scales before the transformation of the surface by the adsorption of species.

On the other hand, other researchers modeled the interactions of metal ions in a liquid solution with γ-alumina

solids at unsteady state [3, 8, 9, 23–26, 38, 39]. Most of these studies assumed the adsorption to reach an instantaneous equilibrium on only one type of OH sites and modeled it using the Langmuir adsorption isotherm. They also described the diffusion using Fick's model, which might not have been the most accurate choice. It is believed that the difference in the self-diffusion coefficients of the cations and anions in solution causes strongly attractive Coulombic forces to act among the ions to maintain the electrical neutrality (i.e., the total charge in the solution should be zero), generating an electrostatic potential along the diffusion path. The gradient of electrostatic potential tends to speed up or slow down the diffusion of ions depending on the sign of their charges and, thus, becomes a force driving the diffusion in addition to the concentration or chemical potential gradient [18]. The zero current method can be used to derive an expression for the electrostatic potential gradient in a solution away from a charged surface. It is an application of the Maxwell–Stefan equation with the condition of electrical neutrality and the no current constraint. For dilute solutions, the zero current method yields the Nernst-Planck equation [16], which has been used by few authors studying γ-alumina [24, 38]. The zero current method has been found to be of sufficient accuracy to capture the essential features of multi-ionic diffusion in solutions inside porous materials [18, 20]. Nevertheless, it does not produce accurate and numerically stable results in cases where charge separation occurs at the surface of non-electrode materials (e.g., the γ-alumina pore surface) [18, 32].

In a very recent study, [16] modeled the diffusion and distribution of species inside concrete structures with positively charged surfaces surrounded by negatively charged hydroxyl ions and contacted with sodium chloride solutions. To do so, they combined two 1 D expressions of: (i) the electrostatic potential $U^{\parallel}$ in the direction parallel to the pore surface (i.e., the diffusion path) using the zero current method and the extended Fick model, and (ii) another electrostatic potential $U^{\perp}$ formed in the EDL in the direction perpendicular to the pore surface using the Poisson-Boltzmann equation. He proposed to use the simple assumption that the activity coefficients are unity (i.e., ideal solutions), which allowed determining the diffusion rates of species inside the pores along with their distribution profiles. He demonstrated that the surface charge, the thickness of the EDL, and the concentrations outside pores all impact the concentration profiles and the diffusion rates inside pores. He found the concentration of cations inside the pores to be less than that outside pores in the case of a positively charged surface, due to the short-range repulsive Coulombic forces exerted by the surface. Nevertheless, this approach does not take into consideration the adsorption of the ions inside the EDL and near the solid surface.

Hence, it is clear that there is a lack of studies devoted to the simultaneous adsorption of protons and metallic cations on several types of active OH sites on the γ-alumina pore surface, while accounting for the effect of the multi-ionic diffusion and of the surface charges on the penetration rates of the species inside pores and their distribution at the liquid/solid interface at unsteady state. The majority of the aforementioned studies also fail in elucidating the effect of the pH and the ionic strength of the liquid solution on the adsorption efficiency and the species distributions inside pores. In this paper, the diffusion and adsorption of protons is modeled inside γ-alumina structures contacted with water at different pH levels in the absence of adsorbing metallic cations. A similar approach to the one used by [16] is used here to model the diffusion of species inside the pores and their distribution inside the EDL. To account for the proton adsorption on the pore surface, the Langmuir adsorption isotherm is applied to three different types of active OH groups that are initially negatively charged and with no competition between them. To validate the model and analyze the effect of the solution pH on the charging behavior of the OH sites on the pore surface, proton adsorption experiments from acid solutions with different initial pH values on previously wetted γ-alumina extrudates are performed in a batch system.

2 Experimental

2.1 Materials

Mineral Mont Roucous water is used to prepare the adsorption solutions and hydrate the alumina extrudates. This water is selected for its limited reaction with carbon dioxide from the surrounding air (due to its minimal mineral content), as opposed to distilled water, which prevents significant pH fluctuations over time [27]. Nitric acid (or HNO_3) puriss. p.a.,≥ 65 % (T) from Sigma-Aldrich is used for the adjustment of the pH (or the proton concentration) of the adsorption solutions. Cylindrical γ-alumina extrudates prepared by the calcination of boehmite at 600 °C are provided by IFPEN. The physical characteristics of the alumina extrudates are provided in Table 1.

2.2 Protocol of proton adsorption experiments

Adsorption solutions with the chosen initial pH are prepared by adding an adequate volume of nitric acid to 260 mL of bottled water. The adsorption experiments are all conducted at room temperature in a batch system consisting of a glass beaker with a magnetic stirring system that does not damage the extrudates (stirring rate of 650 rpm). Mettler Toledo Seven Direct SD23 pH/conductivity-meter with an InLab

Table 1 Physical characteristics of the alumina extrudates (as determined by nitrogen adsorption, mercury porosimetry, and ^{1}H PFG-NMR analysis)

Radius, R_e (mm)	7.20×10^{-1}
Average length, L (mm)	6.70
Specific surface area, S_{BET} (m^{2}g^{-1})	$2.34 \times 10^2 \pm 23.40$
Pore volume, V_{BJH} (mL g^{-1})	$6.10 \times 10^{-1} \pm 6.00 \times 10^{-2}$
Mean pore radius, R_p (nm)	$4.60 \pm 1.80 \times 10^{-1}$
Porosity, ε_p (%)	66 ± 3.30
Tortuosity, τ (−)	$1.97 \pm 3.00 \times 10^{-2}$
Apparent density, $\rho_{alumina}$ (g mL^{-1})	$1.18 \pm 6.00 \times 10^{-2}$

Fig. 1 Schematic representation of the interface between the extra- and intra-granular liquid phases and the distribution of the concentration of a species i at this interface

Expert Pro-ISM pH probe and an InLab 731-ISM conductivity probe (both with external diameters of 12 mm) are used for the online measurement of the pH and the conductivity. 1 g of alumina extrudates are weighed (which corresponds to a dry weight of alumina of $6.20 \times 10^{-1} \pm 1.00 \times 10^{-2}$ g) and pre-hydrated in bottled water for around 2 min. Then, they are removed, and their external surface is carefully dried with a cloth before placing them in the acid solution and starting the pH and conductivity measurements. A schematic representation of the experimental setup is provided in Online Resource 1. The data retrieved from these measurements is used to optimize and validate the model described in the following section. In total, three experiments are conducted at initial proton concentrations in the extra-granular liquid phase of 1.10×10^{-2}, 5.70×10^{-1}, and 4.57 mol m^{-3} (corresponding to pH values of 4.96, 3.24, and 2.34, respectively).

3 Modeling

The system under consideration consists of a volume V_s of cylindrical alumina extrudates all having the same radius R_e, length L, porosity ε_p and tortuosity τ, and confined in a fixed liquid volume V_f containing the following ionic species: protons or H$^+$, nitrate or NO$_3^-$ counter-ions, and hydroxide or OH$^-$ counter-ions. The model is based on material balance equations expressed within the four following domains: (1) the liquid phase outside of the extrudates called the extra-granular liquid phase, referred to as f; (2) the liquid phase inside the extrudate pores called the intra-granular liquid phase, referred to as p; (3) the electrostatic liquid double layer in contact with the pore surface, referred to as EDL; and (4) the adsorbed species on the pore surface.

3.1 Extra-granular liquid phase

The extra-granular liquid is assumed to be a perfectly mixed and closed system, the only outlet being the mass transfer from the extra-granular liquid to the intra-granular liquid. Thus, the material balance of any species i in the extra-granular liquid is expressed as follows:
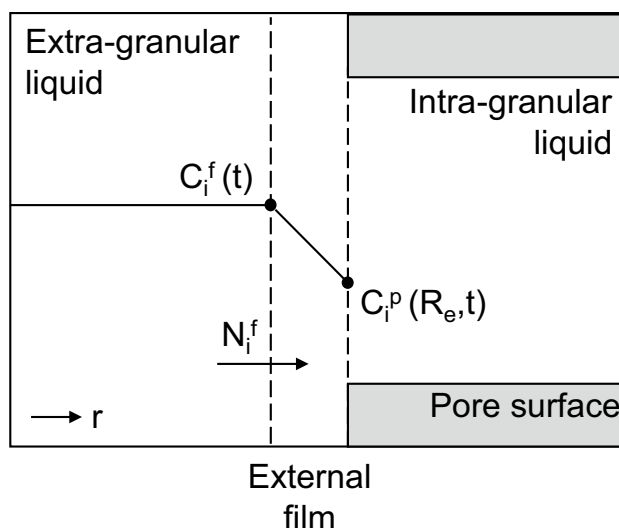
$$\frac{dC_i^f(t)}{dt} = -\frac{2}{R_e}.\varepsilon_p.\frac{V_s}{V_f}.N_i^f(t) \tag{1}$$

where t is the time; C_i^f is the molar concentration of the species i in the extra-granular liquid; and N_i^f is the external molar flux of i between the extra- and intra-granular liquid phases. The latter is assumed to follow the linear film model, so it can be expressed as in Eq. 2:

$$N_i^f(t) = K^f.\left(C_i^f(t) - C_i^p\left(r = R_e, t \right) \right) \tag{2}$$

where K^f is the external mass transfer coefficient and $C_i^p\left(r = R_e, t \right)$ is the molar concentration of i in the intra-granular liquid at the radial position $r = R_e$ (i.e., extrudate surface).

At the extra-granular/intra-granular liquids interface presented in Fig. 1, the mass transfer is assumed to be non-limiting so K^f has the same value for all the species.

Equation 1 is written for H$^+$ and NO$_3^-$. To calculate C_{OH}^f, OH$^-$ ions are assumed to originate from the continuous dissociation reaction of water according to the following equilibrium:

$$H^+ + HO^- \leftrightarrow H_2O$$

C_{OH}^f is determined using the equilibrium constant for this reaction or the water dissociation constant K_w, which is fixed at 10^{-14} mol^{2}L^{-2} at 25 °C [11] and is expressed as follows:

$$K_w = C_H^f(t).C_{OH}^f(t) \tag{3}$$

3.2 Intra-granular liquid phase

When the species leave the extra-granular liquid phase, they are transported by molecular diffusion inside the liquid phase contained inside the porous volume of the extrudates (referred to as the intra-granular liquid phase) according to a molar flux N_i^p. This porous volume is assumed to be a set of cylinders oriented according to the extrudate radial position r, with $0 < r < R_e$ (R_e being the extrudate external radius). Since the pores are assumed to be very long with respect to their diameter, the diffusion is assumed to occur only in the radial direction r [39].

In order to account for the fact that the cylindrical pores are not straight, a tortuosity factor is introduced in the expression of the molar flux N_i^p in the r direction as it is classically done for mass transfer modeling in porous media. In this study, a single alumina support is modeled, so no influence of pore size may be drawn. The possible effect of the pore size is hidden in the tortuosity factor that has been determined by ^{1}H PFG-NMR of toluene in liquid phase (Table 1). Similarly to toluene, water, H^+, OH^-, and NO_3^- are small molecules compared to the mean pore diameter of alumina (9.4 nm as measured by mercury porosimetry) so that no pore size effect is expected.

The corresponding material balance of a component i is [4]:

$$\frac{\partial C_i^p(r,t)}{\partial t} + \frac{1}{r}.\frac{\partial\left[r.N_i^p(r,t)\right]}{\partial r} = -\frac{1}{1-\varepsilon_f}.N_i^{EDL}(r,t).a_p \tag{4}$$

where ε_f is the fraction of the porosity occupied by the EDL; N_i^{EDL} is the internal molar flux of species i between the intra-granular liquid and the EDL surface; and a_p is the pore surface area per unit of pore volume or the interfacial pore area.

The EDL is composed of the pore surface as well as a thin liquid film (see Sect. 3.3 below). This EDL is assumed to be at an internal equilibrium state but is not necessarily at equilibrium with the intra-granular liquid phase. Consequently, a molar flux N_i^{EDL} is introduced for any component i between the intra-granular liquid phase and the EDL surface and is expressed according to the linear film model in Eq. 5.

$$N_i^{EDL}(r,t) = K^{EDL} \cdot \left(C_i^p(r,t) - C_i^{film}(r,t) \right) \tag{5}$$

where K^{EDL} is the internal mass transfer coefficient assumed to have the same value for all species and C_i^{film} is the concentration of species i at the interface between the intra-granular liquid and the EDL surface. a_p is given by the following equation:

$$a_p = \frac{1}{\varepsilon_p}.S_{BET}.\rho_{alumina} \tag{6}$$

The intra-granular liquid phase is an electrolytic solution of charged ionic species diffusing in the water solvent. The diffusion is driven by the chemical potential and electrostatic potential gradients, as indicated in the introduction [18]. The molecular diffusion flux N_i^p is, thus, expressed away from the solid surface in Eq. 7 based on the extended Fick model and the zero-current method described by [20]. It includes two separate terms for each of the two driving forces.

$$N_i^p(r,t) = -D_{eff,i}^p \cdot \left(\frac{\partial C_i^p(r,t)}{\partial r} \right.$$
$$+ C_i^p(r,t).\frac{\partial ln\gamma_i^p(r,t)}{\partial r}$$
$$\left. + v_i.\frac{F}{R.T}.C_i^p(r,t).\frac{\partial U^{\|}(r,t)}{\partial r} \right) \tag{7}$$

where $D_{eff,i}^p$ is the effective diffusion coefficient of i, which is the ratio of the molecular diffusion coefficient in water (or $D_{m,i}^p$) to the tortuosity τ of the porous solid; γ_i^p is the activity coefficient of i in the intra-granular liquid; v_i is the valence of the species i; F is Faraday's constant; R is the ideal gas constant; T is the temperature of the solution; and $U^{\|}$ is the electrostatic potential defined in the direction r parallel to the pore surface and $\frac{\partial U^{\|}}{\partial r}$ is its gradient [16].

The activity coefficient is determined using the Davies thermodynamic model valid for solutions with ionic strengths less than [34]. The solutions used in the experiments with initial H^+ concentrations of 1.10×10^{-2}, 5.70×10^{-1}, and 4.57 molm^{-3} have ionic strengths of 11.48×10^{-6}, 5.62×10^{-4}, and 4.57×10^{-3} M, respectively; which are in the range of validity of the Davies model.

$$log\gamma_i^p(r,t) = \frac{Av_i^2\sqrt{I^p(r,t)}}{1 + \sqrt{I^p(r,t)}} - 0.3\sqrt{I^p(r,t)} \tag{8}$$

where A is the Debye-Hückel constant and I^p is the ionic strength calculated in the intra-granular liquid as follows:

$$I^p(r,t) = \frac{1}{2} \cdot \sum_{i=1}^{n} v_i^2.C_i^p(r,t).10^{-3} \tag{9}$$

where n is the total number of ionic species present in solution.

The expression of $\frac{\partial U^{\|}}{\partial r}$ is developed based upon the fact that there is no external electrical field applied to the system (i.e., the zero-current method), which infers the following constraint on the molecular diffusion flux:

$$\sum_{i=1}^{n} v_i N_i^p(r,t) = 0 \tag{10}$$

Combining Eqs. 7 and 10, yields the following expression for the electrostatic potential gradient:

$$\frac{\partial U^{\parallel}(r,t)}{\partial r} = \frac{\sum_{i=1}^{n} \left[v_i . D_{eff,i}^p \left(\frac{\partial C_i^p(r,t)}{\partial r} \right) + C_i^p(r,t).v_i.D_{eff,i}^p \left(\frac{\partial ln\gamma_i^p(r,t)}{\partial r} \right) \right]}{\sum_{i=1}^{n} \left[\frac{F}{R.T}.v_i^2.D_{eff,i}^p.C_i^p(r,t) \right]} \tag{11}$$

Two boundary conditions are needed to solve Eq. 4:

– at the center of the extrudate, there is no diffusion flux:

$$N_i^p(r=0,t) = 0 \tag{12}$$

– sat the surface of the extrudate, the molar flux in the extra-granular liquid phase equals the molecular diffusion flux in the intra-granular liquid phase:

$$-N_i^p\left(r=R_e,t\right) = K^f \cdot \left(C_i^f(t) - C_i^p\left(r=R_e,t\right) \right) \tag{13}$$

3.3 Concentrations in the EDL and the Poisson-Boltzmann equation

3.3.1 Concentrations in the liquid part of the EDL

At the liquid/solid interface, an EDL is created to neutralize the charges on the pore surface. Inside the EDL, the ionic species are distributed based on their charges and an electrostatic potential $U^{\perp}$ is created; both vary in the direction z perpendicular to the pore surface. A schematic representation of the distribution of a species i in the intra-granular liquid phase and the EDL at any radial position r is presented in Fig. 2.

Assuming the EDL is at an equilibrium state and that the solution is ideal, C_i^{EDL} is related to C_i^{film} by the Boltzmann distribution in Eq. 14 [16, 17]:

$$C_i^{EDL}(z,r,t) = C_i^{film}(z=0,r,t).exp\left(-\frac{F.v_i.U^{\perp}(z,r,t)}{R.T} \right) \tag{14}$$

For small values of $\frac{F.v_i.U^{\perp}(z,r,t)}{R.T}$, Eq. 14 can be approximated by Eq. 15 at any position z:

$$C_i^{EDL}(z,r,t) \approx C_i^{film}(z=0,r,t) \cdot \left(1 - \frac{F.v_i.U^{\perp}(z,r,t)}{R.T} \right) \tag{15}$$

Gauss' law expressed in Eq. 16 is used to determine the expression of the electrostatic potential [17]:
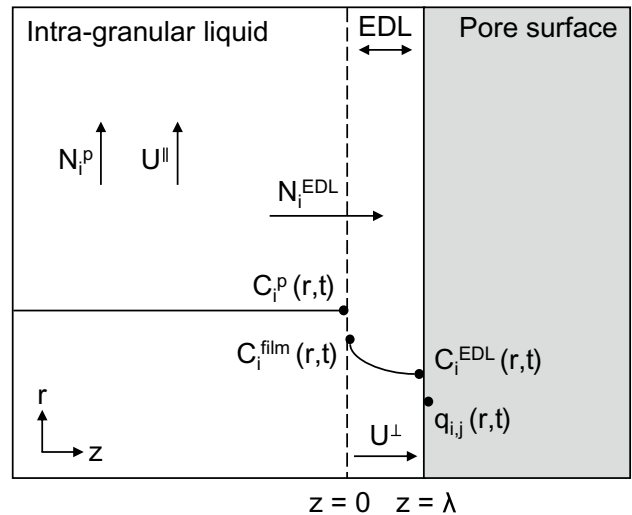
Fig. 2 Schematic representation of the concentration distribution of a species i inside the alumina pores at a radial position r. In the figure, $q_{i,j}$ is the concentration of i adsorbed on the surface site j and C_i^{EDL} is the concentration of i in the EDL

$$\frac{\partial^2 U^{\perp}(z,r,t)}{\partial z^2} = -\frac{\rho(z,r,t)}{\varepsilon} \tag{16}$$

where ρ is the charge density of the liquid part of the EDL expressed in Eq. 17; ε is the permittivity of the water solvent at 25 °C and [17].

$$\rho(z,r,t) = F.\sum_{i=1}^{n} v_i.C_i^{EDL}(z,r,t) \tag{17}$$

Two boundary conditions are needed to solve Eq. 16:

– at the interface between the intra-granular liquid phase and the EDL surface, the electrostatic potential $U^{\perp}$ cancels out [16]:

$$U^{\perp}(z=0,r,t) = 0 \tag{18}$$

– at the interface between the EDL and the pore surface, the application of Gauss' law to a small solid volume containing the pore surface leads to the following equation [17]:

$$\frac{\partial U^{\perp}(z=\lambda,r,t)}{\partial z} = \frac{\sigma(z=\lambda,r,t)}{\varepsilon} \tag{19}$$

where λ is the thickness of the EDL and σ is the surface charge density.

Table 2 Protonation/deprotonation mechanisms of the three surface OH sites accounted for in the model [retrieved from [10]]

Site	Protonation/Deprotonation Mechanism
Site 1	$\mu_1 - OH^{-0.5} + H^+ \rightleftarrows \mu_1 - OH_2^{+0.5}$
Site 2	$\mu_2 - O^{-0.75} + H^+ \rightleftarrows \mu_2 - OH^{+0.25}$
Site 3	$\mu_3 - O^{-0.5} + H^+ \rightleftarrows \mu_3 - OH^{+0.5}$

3.3.2 Concentrations of species adsorbed on the pore surface and the surface charge

H^+ Is the only species that can adsorb on the pore surface, which is known for its heterogeneous nature. For this reason, three types of negatively charged OH sites that are active for H^+ adsorption are assumed to exist on the alumina pore surface according to the adsorption mechanisms described in Table 2 [10]. Note that [10] identify more than three types of OH sites distributed between the predominant (100) and (110) alumina surface planes. However, in this work, only three OH sites are chosen to facilitate the numerical resolution of the model, while still accounting for the heterogeneity of the alumina surface. The OH sites chosen are selected based on the fact that: (i) each one belongs to one of the three main OH groups (μ_1, μ_2, and μ_3) and (ii) they are common between the (100) and (110) alumina surface planes.

In Table 2, $\mu_1 - OH^{-0.5}$, $\mu_2 - O^{-0.75}$, and $\mu_3 - O^{-0.5}$ are the vacant adsorption sites, and $\mu_1 - OH_2^{+0.5}$, $\mu_2 - OH^{+0.25}$, and $\mu_3 - OH^{+0.5}$ are adsorption sites that have adsorbed one H^+ ion each. The H^+ adsorption is assumed to have reached an equilibrium state (i.e., instantaneous adsorption kinetics), so it can be described using the Langmuir adsorption isotherm for any site j:

$$q_{H,j}(z = \lambda, r, t) = \frac{q_{max,j} \cdot b_{H,j} \cdot C_H^{EDL}(z = \lambda, r, t)}{1 + b_{H,j} \cdot C_H^{EDL}(z = \lambda, r, t)} \quad (20)$$

where $q_{H,j}$ is the concentration of H^+ adsorbed on the site j or the concentration of occupied OH sites of the type j on the alumina surface; $q_{max,j}$ is the maximal adsorption capacity of the site j or the maximal number of vacant adsorption sites of type j per unit of surface area; and $b_{H,j}$ is the Langmuir constant or the equilibrium adsorption constant of site j for H^+.

The surface charge on the alumina surface or σ is then given by:

$$\sigma(z = \lambda, r, t) = F \cdot \sum_{j=1}^{N} \left[z_{sj} \cdot \left(q_{max,j} - q_{H,j}(z = \lambda, r, t) \right) + z_j \cdot q_{H,j}(z = \lambda, r, t) \right] \quad (21)$$

where $q_{max,j} - q_{H,j}(z = \lambda, r, t)$ is the concentration of vacant OH sites and N is the number of types of active OH sites (N

is 3 in this case); z_{sj} and z_j are the charges of the vacant and occupied adsorption sites of type j, respectively.

3.3.3 Expression of the electrostatic potential inside the EDL

The Poisson-Boltzmann equation can be solved analytically, and the final expression is obtained for the electrostatic potential $U^\perp$ at any position z inside the EDL:

$$U^\perp(z, r, t) = \frac{\sigma(z = \lambda, r, t)}{\varepsilon} \cdot \frac{1}{\alpha(z = 0, r, t)} \cdot \frac{e^{\alpha(z=0,r,t).z} - e^{\alpha(z=0,r,t).z}}{e^{\alpha(z=0,r,t).\lambda} + e^{\alpha(z=0,r,t).\lambda}} \quad (22)$$

where α is a function of C_i^{film} as follows:

$$\alpha(z = 0, r, t) = \sqrt{\frac{F^2}{\varepsilon.R.T} \cdot \sum_{i=1}^{n} \left(v_i^2 \cdot C_i^{film}(z = 0, r, t) \right)} \quad (23)$$

3.3.4 Global material balance in the EDL

To calculate the time evolution of the species concentrations in the EDL, the material balance in Eq. 24 can be written for H^+:

$$S_{BET} \cdot \rho_{alumina} \cdot \frac{\partial q_H(z = \lambda, r, t)}{\partial t} + \varepsilon_p \cdot \varepsilon_f \cdot \frac{\partial \overline{C}_H^{EDL}(r, t)}{\partial t}$$
$$= S_{BET} \cdot \rho_{alumina} \cdot N_H^{EDL}(z = 0, r, t) \quad (24)$$

where q_H is the total concentration of H^+ adsorbed, which is calculated as the sum of $q_{H,j}$ for the different adsorption sites j ($q_{H,j}$ given by Eq. 20); $\overline{C}_H^{EDL}$ is the mean value of C_H^{EDL} with respect to the z direction expressed in Eq. 25; and N_H^{EDL} is the molar flux of H^+ between the intra-granular liquid phase and the EDL surface as given by Eq. 5.

$$\overline{C}_H^{EDL}(r, t) = \frac{1}{\lambda} \cdot \int_0^{\lambda} C_H^{EDL}(z, r, t) dz \quad (25)$$

For the non-adsorbing species (NO_3^- and OH^-), Eq. 24 is written without the adsorption term (first term to the left-hand side).

3.4 Initial conditions

Three simulations, referred to as Sim 1, Sim 2, and Sim 3, are performed at the same initial H^+ concentrations in the

Table 3 Initial H$^+$ concentrations used in the simulations

Simulation	$C_H^f(t=0)$ (mol m^{-3})	$C_H^p(t=0) = C_H^{film}(t=0)$ (mol m^{-3})
Sim 1	1.10×10^{-2}	1.00×10^{-6}
Sim 2	5.70×10^{-1}	
Sim 3	4.57	

extra-granular liquid phase as the experimental ones. Due to the total dissociation of nitric acid in the extra-granular liquid phase, the concentration of NO$_3^-$ in this same phase is almost equal to the corresponding concentration of H$^+$. The initial concentrations of OH$^-$ in the extra-granular liquid phase, intra-granular liquid phase and internal liquid film are calculated from the water dissociation reaction and the equilibrium constant K_w expressed in Eq. 3.

Only H$^+$ and OH$^-$ are initially present inside the pores due to contacting the alumina extrudates with pure water for a few minutes prior to the adsorption experiments (as indicated in the experimental section). H$^+$ in the intra-granular liquid phase and internal liquid film are assumed to be at an equilibrium state at $t = 0$ min, so the H$^+$ concentration in these two phases are equal. They are given a fixed value of 10^{-6} mol m^{-3} corresponding to an initial pH value inside pores of 9, which is in the range of the point of zero charge (or PZC) of γ-alumina [28].

The initial concentrations of H$^+$ and OH$^-$ in the EDL can be calculated using Eq. 14. Finally, the initial surface charge σ_0 is calculated using Eq. 21 and the initial EDL concentrations of H$^+$ and OH$^-$ (calculated at $z = \lambda$). The initial H$^+$ concentrations used in the simulations are summarized in Table 3. Note that the conditions inside the pores are not well known experimentally, so the values chosen are based on simple assumptions.

A full list of the initial concentrations of the species used in the model for the different phases is presented in Online Resource 2.

3.5 Numerical resolution and estimation of unknown parameters

For each simulation, Eqs. 1, 3, 4, 14, and 24 are applied for each of the species in the system and solved using the implicit ode15i method on MATLAB. To solve Eq. 4, which is a partial differential equation, it is spatially discretized using the central finite differences discretization method [22].

The value of the internal mass transfer coefficient or K^{EDL} is fixed at 5.00×10^{-3} m s^{-1} (so that there is no mass transfer limitation between the intra-granular liquid phase and the EDL), while the fraction occupied by the EDL or ε_f is fixed at 10% of the porosity of the alumina extrudates

(to have a physical meaning relatively to the pore volume). The thickness of the EDL or λ is calculated from ε_f using Eq. 26. To avoid defining this thickness, true 2D Poisson-Boltzmann equations should be used, but they are difficult to solve numerically.

$$\lambda = R_p \left[1 - \sqrt{(1 - \varepsilon_f)} \right] \tag{26}$$

The molecular diffusion coefficients of the different species $D_{eff,i}^p$, the external mass transfer coefficient K^f, and the maximal adsorption capacities $q_{max,j}$ and adsorption constants $b_{H,j}$ of the three surface OH sites, are all estimated by minimizing the squared error between the H$^+$ concentration and the electrical conductivity measured experimentally in the extra-granular liquid phase and the corresponding simulated values, using the non-linear least squares method. The non-linear least squares method used and the calculation of the confidence intervals of the estimated parameters (with a 95% confidence limit) are described in [35]. The results from the experiment with the greatest initial H$^+$ concentration (4.57 mol m^{-3}) are used to estimate the unknown parameters. Whereas the results of the other two experiments are employed for the validation of the model after the parameter estimation, though the value of K^f is re-fitted for each of these two simulations.

The electrical conductivity in the extra-granular liquid phase, which is representative of the total concentration of ionic species present in a solution, is calculated by the model and compared with the experimental data. At dilute conditions, the electrical conductivity EC can be calculated from the concentrations of the species in the extra-granular liquid phase using Eq. 27 [5]:

$$EC(t) = 10^4 \cdot \left[\sum_{i=1}^{n} \left(\Lambda_{m,i} \cdot C_i^f(t) \right) + \Lambda_{m,Al} \cdot 1.306 \times 10^{-5} \cdot t \right] \tag{27}$$

where $\Lambda_{m,i}$ is the molar conductivity of the species i [11].

More details about the choice of Eq. 27 for the conductivity calculations are described in Online Resource 3.

Table 4 Estimated values for the mass transfer parameters of the different species in solution

Parameter	Value	
$D_{m,H}$ (m^{2}s^{-1})	$6.57 \times 10^{-9} \pm 4.22 \times 10^{-9}$	
$D_{m,NO3}$ (m^{2}s^{-1})	$1.08 \times 10^{-9} \pm 4.32 \times 10^{-10}$	
$D_{m,OH}$ (m^{2}s^{-1})	$1.40 \times 10^{-9} \pm 1.62 \times 10^{-9}$	
K^f (m s^{-1})	Sim 1	$5.50 \times 10^{-5} \pm 9.72 \times 10^{-7}$
	Sim 2	$8.00 \times 10^{-6} \pm 4.94 \times 10^{-8}$
	Sim 3	$5.00 \times 10^{-6} \pm 1.99 \times 10^{-7}$

Table 5 Estimated values for the H^+ adsorption parameters

Parameter	Value
$q_{max,1}$ (mol m^{-2})	$7.48 \times 10^{-6} \pm 4.50 \times 10^{-6}$
$q_{max,2}$ (mol m^{-2})	$3.61 \times 10^{-6} \pm 1.49 \times 10^{-6}$
$q_{max,3}$ (mol m^{-2})	$6.59 \times 10^{-6} \pm 2.29 \times 10^{-6}$
$b_{H,1}$ (m^{3}mol^{-1})	40.80 ± 10.28
$b_{H,2}$ (m^{3}mol^{-1})	43.12 ± 9.31
$b_{H,3}$ (m^{3}mol^{-1})	15.66 ± 16.46

4 Results and discussion

4.1 Estimated parameters

The estimated values of the mass transfer and adsorption parameters, along with their confidence intervals are summarized in Tables 4 and 5. It should be noted that the values of the estimated parameters are kept the same for the three simulations except for the external mass transfer coefficient K^f, which value is decreased as the initial H^+ concentration increases, so values of 5.50×10^{-5}, 8.00×10^{-6}, and 5.00×10^{-6} m.s^{-1} are employed for Sim 1, Sim 2, and Sim 3, respectively.

Table 4 shows that H^+ has the greatest molecular diffusion coefficient, followed by the OH^- then the NO_3^- ions, even though all three coefficients are in the same order of magnitude. The estimated values for H^+ and OH^- seem to agree well with the values reported by [9] (9.30×10^{-9} m^{2}s^{-1} for H^+ and 5.30×10^{-9} m^{2}s^{-1} for OH^-, in water at 25 °C) and [2] (7.00×10^{-9} m^{2}s^{-1} for H^+ at ambient temperature). The estimated diffusion coefficient of NO_3^- is close to the value predicted by [38].

In Table 5, the maximal adsorption capacities $q_{max,j}$ for the three different OH sites are in the same order of magnitude. They can be converted into surface densities of OH sites and compared with value calculated in literature. These values are reported in Table 6. The surface densities estimated in this work show some discrepancies with

the other experimental results. This can be explained by different factors, including the strong heterogeneity of the $\gamma-$alumina surface and the initial hydration state of the surface. Remarkably, the surface densities estimated in this work are in close resemblance to the ones determined by [10], except for the surface density of the μ_3 site, which is twice as much in this work.

Finally, the values estimated in this work for the adsorption constants $b_{H,j}$ cannot be compared with values found in literature since significantly different values are reported. Nonetheless, [29, 30] and [10] all found greater protonation constants for the μ_2 sites, followed by the μ_1 and then the μ_3 sites; which is similar to the trend observed in this work. They were able determine the protonation constants of OH sites on the (100) and (110) alumina planes using different approaches: [29] combined the Poisson-Boltzmann equation with the basic Stern model, while [30] and [10] used DFT calculations.

In general, the parameters estimated do not seem to be highly sensitive (especially the adsorption parameters) since they have high uncertainties. In fact, several potential values of these parameters could lead to a good fit between the simulation and the experimental data, but the most reasonable combination is chosen here.
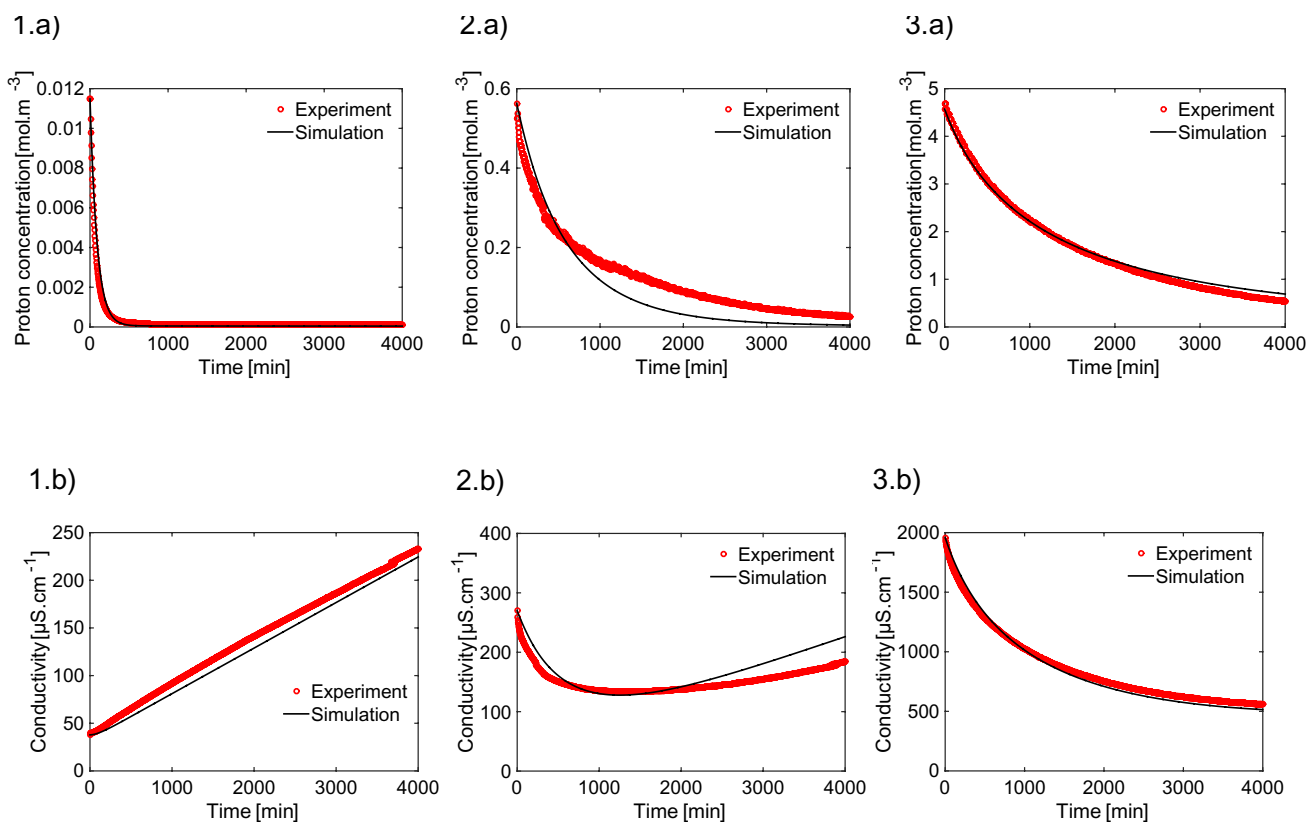
4.2 Simulation data after parameter estimation

The simulation data obtained for Sim 1, Sim 2 and Sim 3 after the parameter estimation are compared with the experimental results for the H^+ concentration and the electrical conductivity in the extra-granular liquid phase presented in Fig. 3.

In general, the simulation data agrees well with the experimental data, as they both follow the same trends and similar values are obtained. The H^+ concentration in the extra-granular liquid phase decreases with time and only stabilizes for Sim 1 after 500 min (Fig. 3-1.a); unlike Sim 2 and Sim 3 where the H^+ concentration never stabilizes (Fig. 3-2.a and -3.a). As the acid solution is contacted with the alumina extrudates, H^+ diffuses inside the solid pores, adsorbs on the pore surface, and is depleted from the extra-granular

Table 6 Comparison of the surface densities of OH sites determined in this work with values reported in literature

OH site	Surface density (nm^{-2})					
	[9]	[29]	[14]	[21]	[10]	This work
μ_1	–	7.20×10^{-1}	–	–	4.31	4.51
μ_2	–	7.20×10^{-1}	–	–	2.16	2.17
μ_3	–	9.60×10^{-1}	–	–	2.16	3.97
Total	7.00×10^{-1} to 1.85 at 25 °C	2.40 at 25 °C	11.80 in (110) plane and 8.80 in (100) plane at 300 °C	8.00 at 200 °C	8.63 at 25 °C	10.65 at 25 °C

1.a)

2.a)

3.a)

1.b)

2.b)

3.b)

Fig. 3 Comparison of the simulation and experimental results for the H^+ concentration (upper plots denoted as a) and electrical conductivity (lower plots denoted as b) in the extra-granular liquid phase, obtained after parameter estimation for initial H^+ concentrations of 1.10×10^{-2} mol m^{-3} (denoted as 1), 5.70×10^{-1} mol m^{-3} (denoted as 2), and 4.57 mol m^{-3} (denoted as 3)

liquid. Interestingly, it appears as though the greater the initial H^+ concentration, the slower is the penetration of H^+ from the extra-granular liquid to the intra-granular liquid. Some papers have shown a decrease in the diffusion of H^+ when the H^+ concentration increases [7, 45].

The behavior of the electrical conductivity in the extra-granular liquid phase is also noteworthy. When the initial H^+ concentration is very low (Sim 1), the electrical conductivity keeps increasing linearly with time, even though the H^+ concentration has long been stabilized (Fig. 3-1.b). However, as the initial H^+ concentration is increased (Sim 2), the conductivity decreases at the beginning almost at the same rate as the experimental data but starts to increase again after 1500 min, slightly deviating from the experimental values. During this time, the H^+ concentration keeps decreasing (Fig. 3-2.b). For the highest initial H^+ concentration (Sim 3), the conductivity decreases slowly as the H^+ concentration also decreases (Fig. 3-3.b).

To understand the trends observed in Fig. 3, the evolution of the simulated concentrations of the different species in the extra-granular liquid phase are compared in Fig. 4. The model shows that the concentration of NO_3^- in the

extra-granular liquid phase decreases at almost the same rate as the H^+ concentration, for the three initial H^+ concentrations tested. This proves that both H^+ and NO_3^- penetrate inside the solid pores so that the electrical neutrality is maintained, regardless of the initial H^+ concentration. Conversely, the concentration of OH^- increases while maintaining small values in comparison with H^+ and NO_3^-. Small amounts of OH^-, which are initially present in very small quantities, are generated in the extra-granular liquid phase by the continuous water dissociation reaction accounted for using Eq. 3. The higher the H^+ concentration in the extra-granular liquid phase, the lower is the concentration of OH^- in the same phase. Hence, it is understandable that the conductivity decreases with time as the H^+ and NO_3^- are being depleted from the extra-granular liquid, as is the case for Sim 3 and the first 1500 min of Sim 2.

Nonetheless, the fact that the conductivity increases in Sim 1 and after 1500 min in Sim 2, might be due to the alumina dissolution generating charged aluminum ions in the extra-granular liquid phase, which is not accounted for in the model except in the conductivity calculations (refer to Eq. 27 and Online Resource 3). The contribution of these aluminum
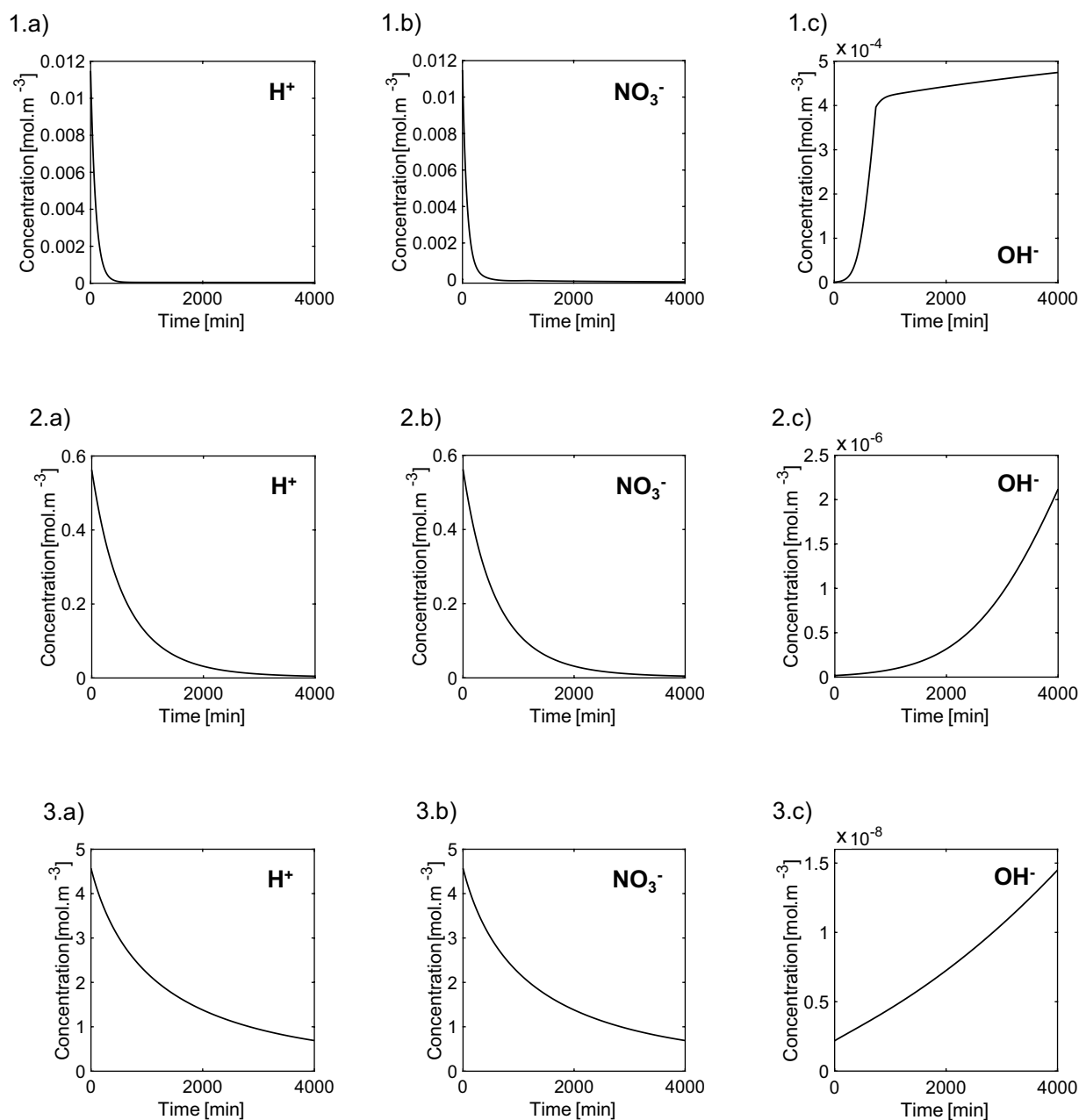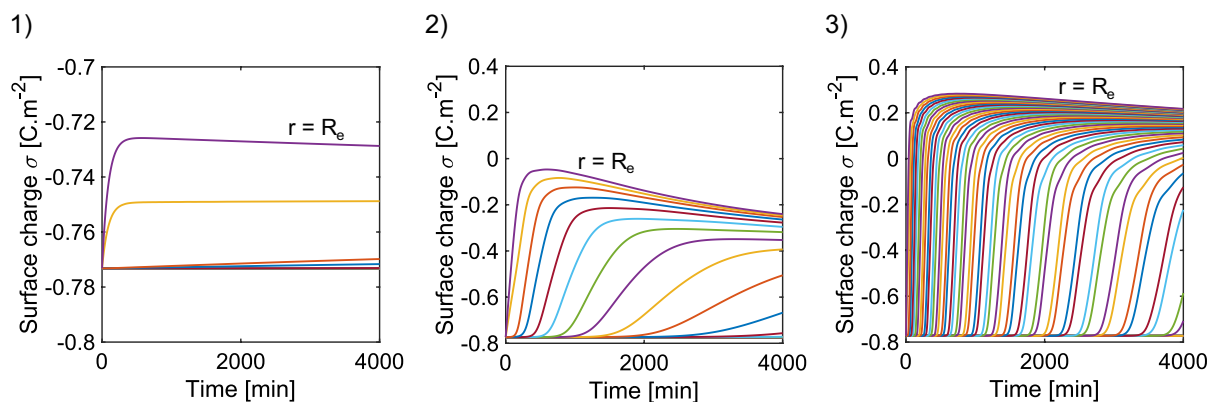
Fig. 4 Simulation results for the H^+ (denoted as a), NO_3^- (denoted as b), and OH^- (denoted as c) concentrations in the extra-granular liquid phase, for initial H^+ concentrations of 1.10×10^{-2} mol m^{-3} (denoted as 1), 5.70×10^{-1} mol m^{-3} (denoted as 2), and 4.57 mol m^{-3} (denoted as 3)

ions to the conductivity might be unnoticeable when greater amounts of H^+ and NO_3^- are present in solution (the first 1500 min of Sim 2 and throughout Sim 3). Two competing phenomena are affecting the evolution of the electrical conductivity in the extra-granular liquid phase: (i) the proton adsorption causing the decrease of the conductivity and

(ii) the alumina dissolution that causes the conductivity to increase. In the case of Sim 2, the operating conditions are such that the competition between these two phenomena is clearly observed.

Moreover, depending on the solution pH, the aluminum ions generated in the extra-granular liquid phase can have

Fig. 5 Simulation results for the charge on the alumina surface, for initial H^+ concentrations of 1.10×10^{-2} mol m^{-3} (denoted as 1), 5.70×10^{-1} mol m^{-3} (denoted as 2), and 4.57 mol m^{-3} (denoted as 3). The curves marked by $r = R_e$ corresponds to the extrudate surface

different hydration levels, each contributing to the overall conductivity differently [41]. Thus, the corrective term for the rate of alumina dissolution added to the calculation of the conductivity in Eq. 27, might be inaccurate especially for Sim 2; the rate of alumina dissolution could be overestimated, non-linear, and pH dependent.

4.3 Time variations of the surface charge

The charge on the alumina surface σ is calculated at different radial positions inside extrudates using Eq. 21. The results obtained for the three initial H^+ concentrations tested are presented in Fig. 5 as a function of time and the radial positions r inside the extrudates (from the extrudate center at $r = 0$ to its external surface at $r = R_e$).

At $t = 0$ min, the surface charge σ_0 has a value of -0.77 Cm^{-2} for Sim 1, Sim 2, and Sim 3, as the same initial concentrations are used for the three simulations. They all show an increase in the surface charge with time, even though the increase observed in Sim 1 is minor compared to the other simulations. This is due to the H^+ adsorption, which makes the charge of the OH sites more positive. The increase of σ is slower at the radial positions closer to the extrudate center, as H^+ takes longer to diffuse towards the center. In fact, so little H^+ reaches the center of the extrudates that the surface charge is almost unchanged at these positions even after 4000 min, for all three initial H^+ concentrations.

The surface charge stabilizes and approaches an equilibrium state at the radial positions near the extrudate surface. With the highest initial H^+ concentration (Sim 3), the total surface charge becomes positive at the radial positions reached by the H^+ adsorption after 4000 min. This shows that, in these cases, the concentration of H^+ adsorbed on the alumina surface is big enough to make the total surface charge positive. Moreover, surface charges obtained in Sim

3 at t = 4000 min reaches values of 0.2 − 0.3 Cm^{-2} for different radial positions inside the extrudates. These values are comparable with the findings of [10, 29]. Reference [29] predicted total surface charges of around −0.25 and 0.25 C.m^{-2} at equilibrium H^+ concentrations of 0.02 and 1 molm^{-3}, respectively, using the Poisson-Boltzmann equation and experimental data of alumina powders contacted with acidic sodium nitrate solutions for 24 h. On the other hand, [10] determined a surface charge in the order of 0.05 C.m^{-2} by potentiometric titration experiments of alumina powders at pH = 5, room temperature, and an ionic strength of 1 mM. Note that the ionic strength at t = 4000 min is 0.64 mM for Sim 3.

4.4 Time variations and spatial profiles of concentrations in the intra-granular liquid phase, the EDL, and the solid surface

The simulated concentrations of the different species inside the pores are presented for the three simulations in Figs. 6, 7 and 8. The model can predict both the time variations and spatial profiles of the species in the various phases.

The H^+ concentrations in the intra-granular liquid phase and the EDL increase with time for the three simulations (Fig. 6), as the H^+ concentration decreases in the extra-granular liquid phase (Fig. 4). Once it reaches the EDL, the H^+ adsorbs on the pore surface, also increasing the concentration of H^+ adsorbed q_H. The greater the initial concentration of H^+ in the extra-granular liquid phase, the greater are the values of C_H^p, C_H^{EDL} and q_H and the faster is their evolution. For the cases with the lower initial H^+ concentrations (Sim 1 and 2), more H^+ are available in the EDL than in the intra-granular liquid phase to neutralize the negative surface charge. In contrast, when the initial H^+ concentration is high (Sim 3), H^+ is mostly concentrated in the intra-granular liquid phase and not in the EDL since the positively charged
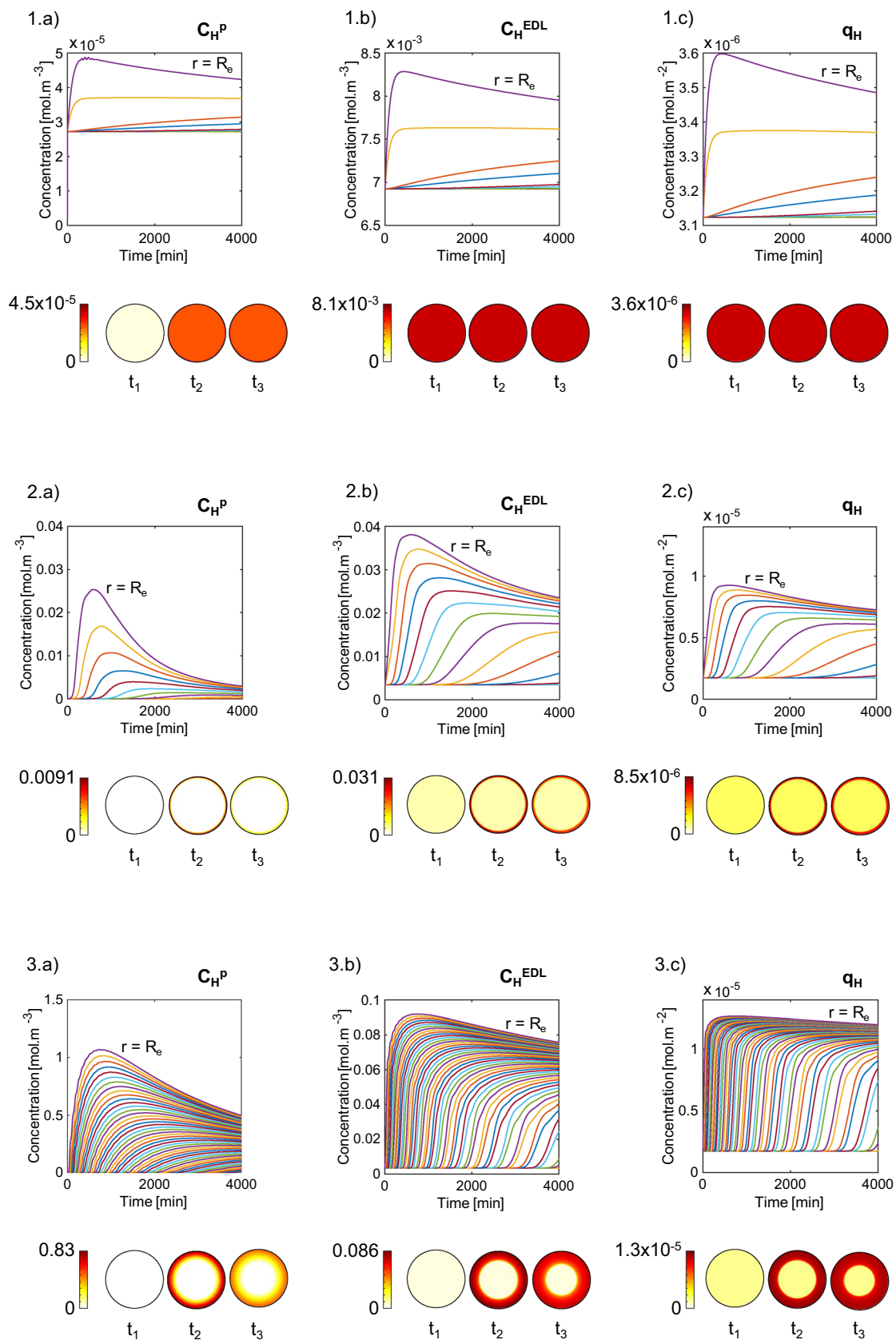
◀**Fig. 6** Simulation results of the evolution of the H$^+$ concentration in the intra-granular liquid phase C_H^p (denoted as a), its concentration in the EDL C_H^{EDL} (denoted as b), and that adsorbed on the pore surface q_H (denoted as c), for initial H$^+$ concentrations of 1.10×10^{-2} mol m^{-3} (denoted as 1), 5.70×10^{-1} mol m^{-3} (denoted as 2), and 4.57 mol m^{-3} (denoted as 3). The curves marked by $r = R_e$ correspond to the extrudate surface. The circular plots under each graph represent the spatial profiles of the concentration in the same phase after $t_1 = 0$ min, $t_2 = 2000$ min and $t_3 = 4000$ min. The color bars are expressed in mol m^{-3}

H$^+$ ions are repulsed by the positively charged surface. The spatial profiles also show that the penetration depth of H$^+$ depends on the initial conditions, as H$^+$ can penetrate deeper inside extrudates when greater initial H$^+$ concentrations are provided. Nevertheless, H$^+$ in the intra-granular liquid phase does not reach the extrudate center in any of the cases studied, while very small amounts in the EDL reach the center; in other terms, the H$^+$ diffusion is very slow. It is also noteworthy that, regardless of its initial concentration, as H$^+$ penetrates deeper inside the extrudates, its concentrations in the intra-granular liquid phase, the EDL, and adsorbed on the pore surface increase and then slightly decrease near the extrudate edges between 0 and 4000 min. It should be noted that, since the model predicts the local concentration of H$^+$, it can give a local measure of the pH inside the alumina pores.

Figure 7 shows that the NO$_3^-$ concentrations increase with time in the intra-granular liquid phase and the EDL. The greater the initial H$^+$ concentration, the greater is the NO$_3^-$ concentration and the faster is the increase, as observed for H$^+$. However, greater NO$_3^-$ concentrations are predicted in the intra-granular liquid phase than in the EDL for Sim 1 and 2, in contrast with H$^+$. This can only be explained by the repulsion of the NO$_3^-$ ions by the negatively charged surface. The opposite trend is observed in Sim 3, where the surface becomes positively charged. The penetration depth of NO$_3^-$ into the intra-granular liquid phase and the EDL increases with time, even though their concentration near the extrudate edges slightly decreases, and they never reach the extrudate center.

The three simulations exhibit a decrease in the OH$^-$ concentration in the intra-granular liquid phase with time (though the change is not pronounced in Sim 1) and an increase in the concentration in the EDL (Fig. 8). The greater the initial H$^+$ concentration, the greater is the decrease of the OH$^-$ concentration in the intra-granular liquid phase and its increase in the EDL. The decrease in the concentration in the intra-granular liquid phase is also evident in the spatial profiles that display lower OH$^-$ concentrations in this phase near the extrudate edges and the thickness of the band of low concentration increases with time. The OH$^-$ ions are, thus, expelled from the intra-granular liquid phase to the EDL and/or the extra-granular liquid phase (Fig. 8 shows a decrease in the OH$^-$ concentration in the intra-granular liquid phase for the three simulations). The same trend for the distribution of concentrations between the intra-granular liquid phase and the EDL as the NO$_3^-$ is observed in this case; the concentration of OH$^-$ in the intra-granular liquid is greater than in the EDL in Sim 1 and 2 and lower in Sim 3.

Comparing the concentrations of the different species in the intra-granular liquid phase shows that H$^+$ and NO$_3^-$ exhibit similar trends for the time variations, concentration values, and spatial profiles. Note that Fig. 4 also shows both ions evolving similarly in the extra-granular liquid phase. NO$_3^-$ seems to follow H$^+$ in both the extra-granular and intra-granular liquid phases. OH$^-$ undergoes the opposite behavior as H$^+$ and NO$_3^-$; the concentration of OH$^-$ decreases in the regions where the H$^+$ and NO$_3^-$ concentrations increase. The most probable explanation is that the electrical neutrality in the intra-granular liquid phase is satisfied when the total concentrations of the negatively charged ions (i.e., NO$_3^-$ and OH$^-$) equals the concentration of the positively charged ions (i.e., H$^+$). Since the NO$_3^-$ concentration is very close to the H$^+$ concentration, OH$^-$ is expelled from this phase. On the other hand, in the EDL, the evolutions of H$^+$, NO$_3^-$ and OH$^-$ occur at different rates. In Sim 1 and 2, greater concentrations of H$^+$ are recorded in EDL compared to NO$_3^-$ and OH$^-$. In Sim 3, the concentration of H$^+$ in the EDL is lower than that of NO$_3^-$, yet greater than that of OH$^-$. The spatial profiles of the three species seem to have the same tendencies. This behavior can be explained by the distribution of H$^+$, NO$_3^-$ and OH$^-$ in the EDL required to neutralize the surface charge σ and maintain the electrical neutrality, as imposed by the Poisson-Boltzmann equation. As a result, in the case of Sim 1 and 2 where the initial H$^+$ concentration is low and the surface charge σ remains negative (Fig. 5), the positively charged H$^+$ ions are attracted by the solid surface towards the EDL and the negatively charged NO$_3^-$ and OH$^-$ ions are repelled from it. In contrast, in Sim 3, H$^+$ is repelled by the positively charged surface to the intra-granular liquid phase and NO$_3^-$ and OH$^-$ are concentrated in the EDL.

It should be noted that the calculation of the activity coefficients of the ionic species using Eq. 8 yields values very close to unity throughout the time span of the simulations (i.e., 4000 min). This shows that the liquid solution exhibits a nearly ideal behavior for all species in all the phases at the pH conditions studied in this work.

Fig. 7 Simulation results of the evolution of the NO_3^- concentration in the intra-granular liquid phase $C_{NO_3}^p$ (denoted as a) and its concentration in the EDL $C_{NO_3}^{EDL}$ (denoted as b), for initial H^+ concentrations of 1.10×10^{-2} mol m^{-3} (denoted as 1), 5.70×10^{-1} mol m^{-3} (denoted as 2), and 4.57 mol m^{-3} (denoted as 3). The curves marked by $r = R_e$ correspond to the concentrations at the extrudate surface. The circular plots under each graph represent the spatial profiles of the concentration in the same phase after $t_1 = 0$ min, $t_2 = 2000$ min and $t_3 = 4000$ min. The color bars are expressed in mol m^{-3}
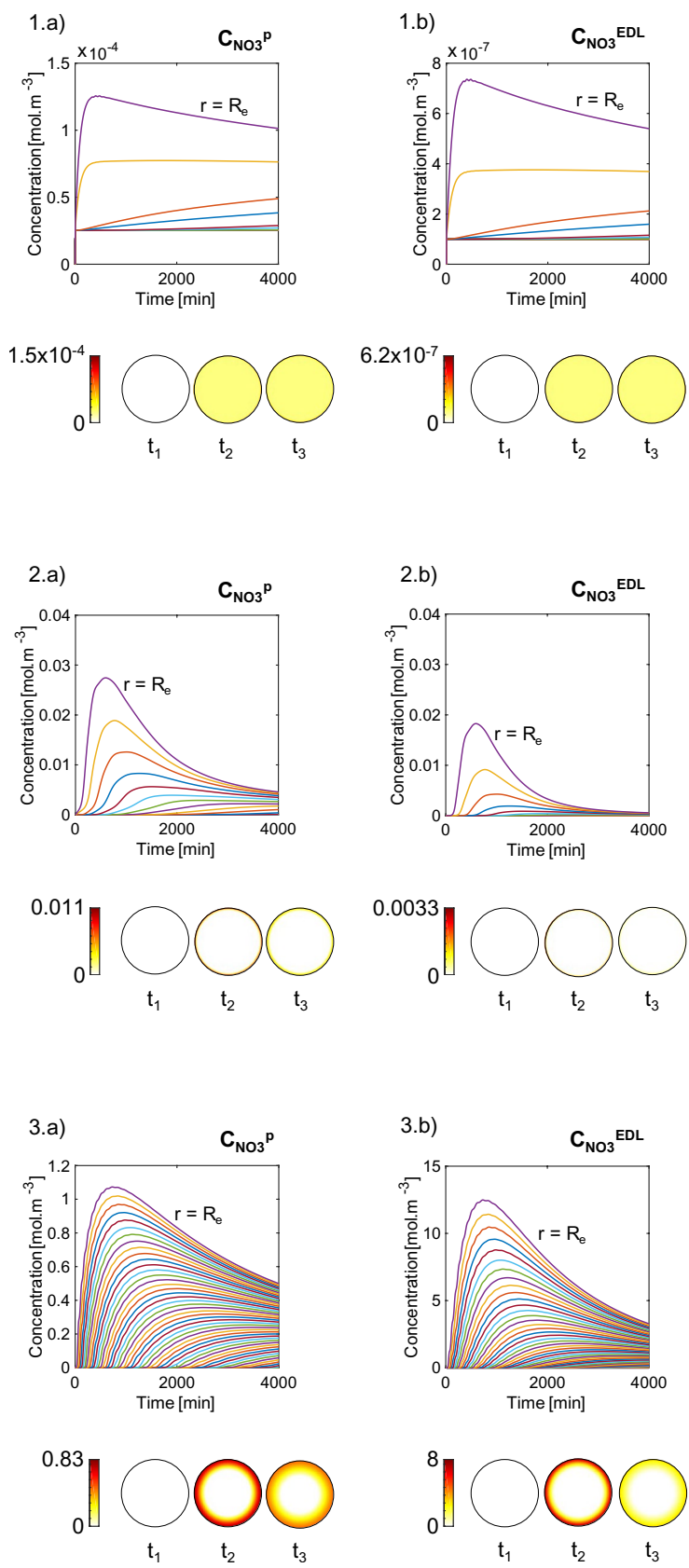
Fig. 8 Simulation results of the evolution of the OH⁻ concentration in the intra-granular liquid phase C_{OH}^p (denoted as a) and its concentration in the EDL C_{OH}^{EDL} (denoted as b), for initial H⁺ concentrations of 1.10×10^{-2} mol m⁻³ (denoted as 1), 5.70×10^{-1} mol m⁻³ (denoted as 2), and 4.57 mol m⁻³ (denoted as 3). The curves marked by $r = R_e$ correspond to the concentrations at the extrudate surface. The circular plots under each graph represent the spatial profiles of the concentration in the same phase after $t_1 = 0$ min, $t_2 = 2000$ min and $t_3 = 4000$ min. The color bars are expressed in mol m⁻³
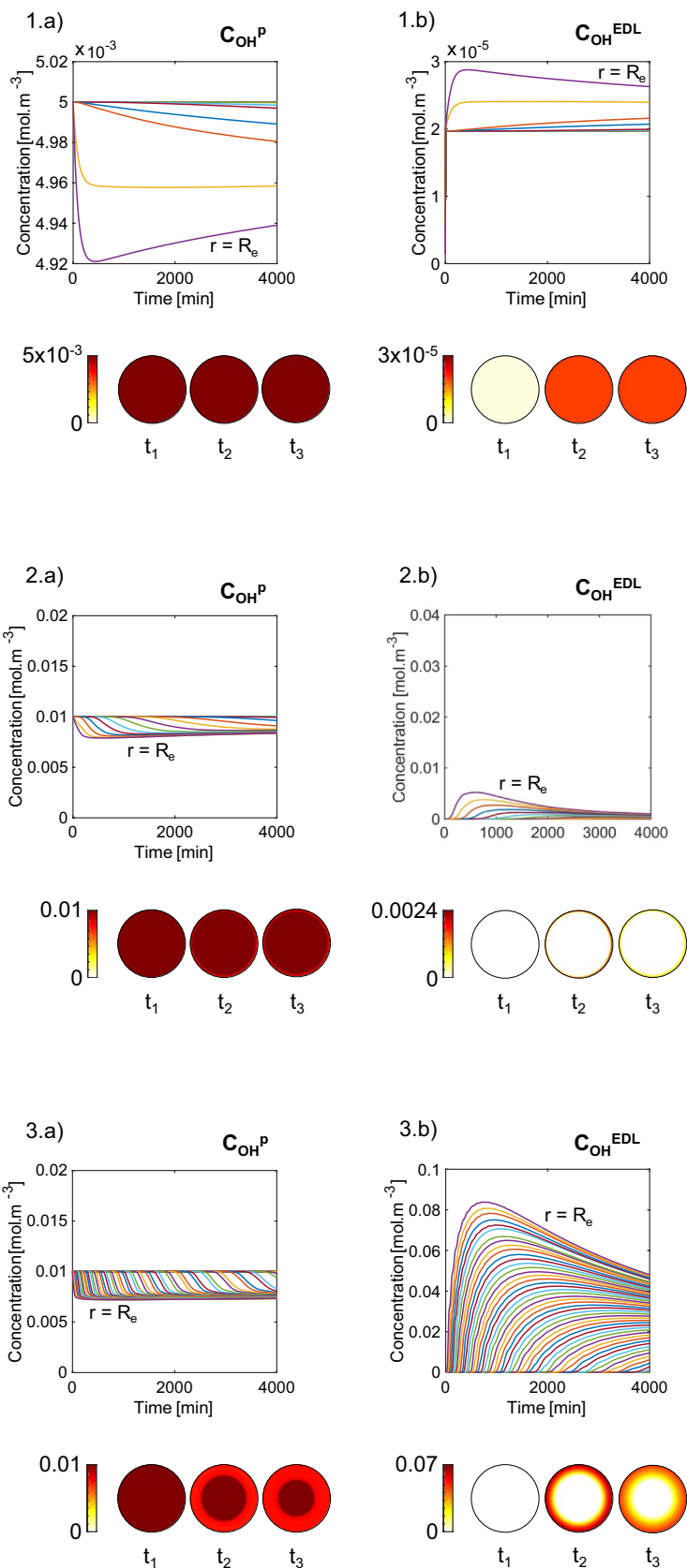
5 Conclusion

In this article, a model is proposed for the simultaneous ionic diffusion of three different ions (H^+, NO_3^- and OH^-) inside the pores of charged alumina extrudates and the adsorption of H^+ on this surface. The zero-current method and the Poisson-Boltzmann equation are combined to represent the diffusion of the ionic species in the solution inside the pores and their distribution inside the EDL at unsteady state. The Langmuir adsorption isotherm is used to represent the H^+ adsorption.

The model can accurately predict the concentrations of the different species and the electrical conductivity outside the extrudates, as has evidenced by the good agreement between the simulation data and the results of adsorption experiments conducted in a batch system. The estimated parameters also seem to be coherent with findings in literature regardless of the fact that only experimental data in the extra-granular liquid phase are used for the parameter estimation, which explains the lack of sensitivity for some of the parameters. The model can also compute: i) the density of the various OH sites on the pore surface, ii) the total surface charge, and iii) the concentration gradients of the species inside the pores (in the liquid and adsorbed states) and their dynamic variations (including the local pH), all of which are very difficult to determine experimentally. It can also predict the distribution of the species between the intra-granular liquid phase and inside the EDL formed at the liquid/solid interface to neutralize the charges on the solid surface. NO_3^- ions seem to follow H^+ inside the solid pores, and they are concentrated in the intra-granular liquid when the surface is negatively charged (at low initial H^+ concentrations) or inside the EDL when the surface is positively charged (at high initial H^+ concentrations). Furthermore, the surface charge seems to play a critical role in driving the evolution of the H^+ concentration (and pH) not only in the intra-granular liquid phase, but also in the extra-granular liquid phase.

Finally, this model provides a more rational understanding of the reactivity of the $\gamma-$ alumina surface with aqueous solutions during impregnation and water treatment processes. More generally, this model can also prove useful in the field of surface chemistry and the studies of liquid/solid interfaces inside mineral oxides.

Declarations

References

1. Agashe, K.B., Regalbuto, J.R.: A revised physical theory for adsorption of metal complexes at oxide surfaces. J. Colloid Interface Sci. **185**(1), 174–189 (1997). https://doi.org/10.1006/jcis.4493

2. Agmon, N.: The Grotthuss mechanism. Chem. Phys. Lett. **244**(5–6), 456–462 (1995). https://doi.org/10.1016/0009-2614(95)00905-J

3. Assaf, E.M., Jesus, L.C., Assaf, J.M.: The active phase distribution in Ni/Al$_2$O$_3$ catalysts and mathematical modeling of the impregnation process. Chem. Eng. J. **94**(2), 93–98 (2003). https://doi.org/10.1016/S1385-8947(03)00006-8

4. Bird, R.B., Stewart, W.E., Lightfoot, E.N.: Transport Phenomena, 2nd edn. Wiley, New York (2002)

5. Blaine McCleskey, R., Kirk Nordstrom, D., Ryan, J.N.: Electrical conductivity method for natural waters. Appl. Geochem. **26**, S227–S229 (2011). https://doi.org/10.1016/j.apgeochem.2011.03.110

6. Busca, G.: Structural, surface, and catalytic properties of aluminas. In *Advances in Catalysis* (Vol. 57, pp. 319–404). Elsevier, Amsterdam (2014). https://doi.org/10.1016/B978-0-12-800127-1.00003-5

7. Calio, P.B., Li, C., Voth, G.A.: Molecular origins of the barriers to proton transport in acidic aqueous solutions. J. Phys. Chem. B **124**(40), 8868–8876 (2020). https://doi.org/10.1021/acs.jpcb.0c06223

8. Catita, L., Jolimaitre, E., Quoineaud, A.-A., Delpoux, O., Pichon, C., Schweitzer, J.-M.: Mathematical modeling and magnetic resonance imaging experimental study of the impregnation step: a new tool to optimize the preparation of heterogeneous catalysts. Microporous Mesoporous Mater. **312**, 110756 (2021). https://doi.org/10.1016/j.micromeso.2020.110756

9. Chu, P., Petersen, E.E., Radke, C.J.: Modeling wet impregnation of nickel on γ-Alumina. J. Catal. **117**(1), 52–70 (1989). https://doi.org/10.1016/0021-9517(89)90220-0

10. Corral Valero, M., Prelot, B., Lefèvre, G.: MUSIC speciation of γ-Al$_2$O$_3$ at the solid liquid interface: How DFT calculations can help with amorphous and poorly crystalline materials. Langmuir **35**(40), 12986–12992 (2019). https://doi.org/10.1021/acs.langmuir.9b02788

11. Dean, J.A.: Lange's Handbook of Chemistry, 15th edn. McGraw-Hill Inc, New York (1999)

12. d'Espinose De La Caillerie, J.-B., Kermarec, M., Clause, O.: Impregnation of γ-Alumina with Ni(II) or Co(II) Ions at neutral pH: hydrotalcite-type coprecipitate formation and characterization. J. Am. Chem. Soc. **117**(46), 11471–11481 (1995). https://doi.org/10.1021/ja00151a010

13. Digne, M.: Use of DFT to achieve a rational understanding of acid/basic properties of γ-alumina surfaces. J. Catal. **226**(1), 54–68 (2004). https://doi.org/10.1016/j.jcat.2004.04.020

14. Digne, M., Sautet, P., Raybaud, P., Euzen, P., Toulhoat, H.: Hydroxyl groups on γ-alumina surfaces: a DFT study. J. Catal. **211**(1), 1–5 (2002). https://doi.org/10.1006/jcat.2002.3741

15. Hiemstra, T., Van Riemsdijk, W.H., Bolt, G.H.: Multisite proton adsorption modeling at the solid/solution interface of (hydr) oxides: a new approach. J. Colloid Interface Sci. **133**(1), 91–104 (1989). https://doi.org/10.1016/0021-9797(89)90284-1

16. Ichikawa, T.: Theory of ionic diffusion in water-saturated porous solid with surface charge. J. Adv. Concr. Technol. **20**(7), 430–443 (2022). https://doi.org/10.3151/jact.20.430

17. Israelachvili, J.N.: Intermolecular and Surface Forces, 3rd edn. Elsevier, Amsterdam (2011)

18. Johannesson, B.: Comparison between the Gauss' law method and the zero current method to calculate multi-species ionic diffusion in saturated uncharged porous materials. Comput. Geotech. **37**(5), 667–677 (2010). https://doi.org/10.1016/j.compgeo.2010.04.005

19. Kasprzyk-Hordern, B.: Chemistry of alumina, reactions in aqueous solution and its application in water treatment. Adv. Coll. Interface. Sci. **110**(1–2), 19–48 (2004). https://doi.org/10.1016/j.cis.2004.02.002

20. Krishna, R.: Highlighting coupling effects in ionic diffusion. Chem. Eng. Res. Des. **114**, 1–12 (2016). https://doi.org/10.1016/j.cherd.2016.08.009

21. Lagauche, M., Larmier, K., Jolimaitre, E., Barthelet, K., Chizallet, C., Favergeon, L., Pijolat, M.: Thermodynamic characterization of the hydroxyl group on the γ-alumina surface by the energy distribution function. J. Phys.Chem. C **121**(31), 16770–16782 (2017). https://doi.org/10.1021/acs.jpcc.7b02498

22. Langtangen, P. H.: Finite difference computing with exponential decay models. Springer Nature, Cham (2016)

23. Li, W.D., Li, Y.W., Qin, Z.F., Chen, S.Y.: Theoretical prediction and experimental validation of the egg-shell distribution of Ni for supported Ni/Al$_2$O$_3$ catalysts. Chem. Eng. Sci. **49**(24), 4889–4895 (1994). https://doi.org/10.1016/S0009-2509(05)80067-3

24. Liu, X., Khinast, J.G., Glasser, B.J.: A parametric investigation of impregnation and drying of supported catalysts. Chem. Eng. Sci. **63**(18), 4517–4530 (2008). https://doi.org/10.1016/j.ces.2008.06.013

25. Melo, F., Cervelló, J., Hermana, E.: Impregnation of porous supports—I theoretical study of the impregnation of one or two active species. Chem. Eng. Sci. **35**(10), 2165–2174 (1980). https://doi.org/10.1016/0009-2509(80)85041-X

26. Melo, F., Cervelló, J., Hermana, E.: Impregnation of porous supports—II System Ni/Ba on alumina. Chem. Eng. Sci. **35**(10), 2175–2184 (1980). https://doi.org/10.1016/0009-2509(80)85042-1

27. Mitchell, M.J., Jensen, O.E., Cliffe, K.A., Maroto-Valer, M.M.: A model of carbon dioxide dissolution and mineral carbonation kinetics. Proc. Roy. Soc. A: Math. Phys. Eng. Sci. **466**(2117), 1265–1290 (2010). https://doi.org/10.1098/rspa.2009.0349

28. Munnik, P., De Jongh, P.E., De Jong, K.P.: Recent developments in the synthesis of supported catalysts. Chem. Rev. **115**(14), 6687–6718 (2015). https://doi.org/10.1021/cr500486u

29. Nagashima, K., Blum, F.D.: Proton adsorption onto alumina: extension of multisite complexation (MUSIC) theory. J. Colloid Interface Sci. **217**(1), 28–36 (1999). https://doi.org/10.1006/jcis.1999.6355

30. Ngouana-Wakou, B.F., Cornette, P., Corral Valero, M., Costa, D., Raybaud, P.: An atomistic description of the γ-alumina/water interface revealed by ab initio molecular dynamics. J. Phys. Chem. C **121**(19), 10351–10363 (2017). https://doi.org/10.1021/acs.jpcc.7b00101

31. Nowacka, A., Moughames, J., Adem, Z., Quoineaud, A.-A., Rolland, M., Guenneau, F., Gédéon, A.: In situ magnetic resonance imaging study of the impregnation of γ-alumina pellets. Appl. Catal. A **503**, 111–116 (2015). https://doi.org/10.1016/j.apcata.2015.07.014

32. Park, J., Regalbuto, J.R.: A simple, accurate determination of oxide PZC and the Strong buffering effect of oxide surfaces at incipient wetness. J. Colloid Interface Sci. **175**(1), 239–252 (1995). https://doi.org/10.1006/jcis.1995.1452

33. Parks, G.A.: The isoelectric points of solid oxides, solid hydroxides, and aqueous hydroxo complex systems. Chem. Rev. **65**(2), 177–198 (1965). https://doi.org/10.1021/cr60234a002

34. Prausnitz, J. M., Lichtenthaler, R. N., Gomes de Azevedo, E.: Molecular thermodynamics of fluid-phase equilibria. In: (N. R. Amundson (Ed.), 3rd edn. Prentice Hall PTR, New Jersey (1999).

35. Rasmuson, A., Andersson, B., Olsson, L., Andersson, R.: Statistical analysis of mathematical models. In: Mathematical Modeling in Chemical Engineering. Cambridge University Press, Cambridge (2014).

36. Reocreux, R.: Biomass derivatives in heterogeneous catalysis: Adsorption, reactivity and support from first principles. PhD Dissertation, Université de Lyon (2017).

37. Reocreux, R., Jiang, T., Iannuzzi, M., Michel, C., Sautet, P.: Structuration and dynamics of interfacial liquid water at hydrated γ-alumina determined by ab initio molecular simulations: implications for nanoparticle stability. ACS Applied Nano Materials **1**(1), 191–199 (2018). https://doi.org/10.1021/acsanm.7b00100

38. Ruckenstein, E., Karpe, P.: Control of metal distribution in supported catalysts by pH, ionic strength, and coimpregnation. Langmuir **5**(6), 1393–1407 (1989). https://doi.org/10.1021/la00090a023

39. Scelza, O.A., Castro, A.A., Ardiles, D.R., Parera, J.M.: Modeling of the impregnation step to prepare supported platinum/alumina catalysts. Ind. Eng. Chem. Fundam. **25**(1), 84–88 (1986). https://doi.org/10.1021/i100021a012

40. Spanos, N., Lycourghiotis, A.: Mechanism of deposition of Co^{2+} and Ni^{2+} ions on the interface between pure and F$^-$-doped γ-alumina and the impregnating solution. J. Chem. Soc., Faraday Trans. **89**(22), 4101–4107 (1993). https://doi.org/10.1039/FT9938904101

41. Sparks, D.L., Singh, B., Siebecker, M.G.: Environmental Soil Chemistry, 2nd edn. Elsevier, Amsterdam (2002)

42. Van Riemsdijk, W.H., Bolt, G.H., Koopal, L.K., Blaakmeer, J.: Electrolyte adsorption on heterogeneous surfaces: adsorption models. J. Colloid Interface Sci. **109**(1), 219–228 (1986). https://doi.org/10.1016/0021-9797(86)90296-1

43. Van Riemsdijk, W.H., De Wit, J.C.M., Koopal, L.K., Bolt, G.H.: Metal ion adsorption on heterogeneous surfaces: adsorption models. J. Colloid Interface Sci. **116**(2), 511–522 (1987). https://doi.org/10.1016/0021-9797(87)90147-0

44. Vordonis, L., Spanos, N., Koutsoukos, P. G., Lycourghiotis, A.: Mechanism of adsorption of Co2+ and Ni2+ Ions on the "Pure and Fluorinated γ-Alumina/Electrolyte Solution" interface. **8**, 1736–1743 (1992).

45. Xu, J., Izvekov, S., Voth, G.A.: Structure and dynamics of concentrated hydrochloric acid solutions. J. Phys. Chem. B **114**(29), 9555–9562 (2010). https://doi.org/10.1021/jp102516h

Authors and Affiliations

Rita Fayad[1] · **Yu-Yen Ting[2]** · **Françoise Couenne[1]** · **Christian Jallut[1]** · **Aurelie Galfré[1]** · **Elsa Jolimaitre[3]** · **Loïc Sorbier[4]** · **Charles-Philippe Lienemann[4]** · **Mélaz Tayakout-Fayolle[1]**

✉ Mélaz Tayakout-Fayolle
melaz.tayakout-fayolle@univ-lyon1.fr

1   Univ Lyon, Université Claude Bernard Lyon 1, CNRS,
    LAGEPP UMR 5007, 43 Boulevard du 11 Novembre 1918,
    69100 Villeurbanne, France

2   Kaohsiung, Taiwan, R.O.C.

3   So Sponge, Axel'One Campus, 5 Av. Gaston Berger,
    69100 Villeurbanne, France

4   IFP Energies Nouvelles, Rond-Point de l'échangeur de
    Solaize BP3, 69360 Solaize, France